Research on Engineering Structures & Materials
www.jresm.org
Research Group

Research Article

Multi objective geometry optimization of deep-hole trepanning tools via a reinforcement learning enhanced Grey Wolf optimizer

Feng Guo [*,a], Xuejun Wang [b]

Engineering Training Center, Shandong Huayu University of Technology, Dezhou, China

Article Info

Article History:

Received 17 July 2026

Accepted 14 Aug 2026

Keywords:

Deep-hole trepanning; SORD-RL-MOGWO; Pareto-optimal design; Machinability enhancement; Chip evacuation stability

Abstract

Deep-hole trepanning is challenged by enclosed cutting conditions and limited chip evacuation, leading to increased cutting loads, chip blockage, and reduced tool reliability. These challenges are particularly severe in trepanning because the retained core material confines the annular cutting zone and narrows the chip evacuation path. To optimize the geometric parameters of deep-hole trepanning tools, a constrained multi-objective optimization model is developed to simultaneously minimize axial force, cutting torque, and chip blockage risk, with rake angle, clearance angle, point angle, edge radius, chip-breaker width, and chip-groove guide angle as design variables. To solve this model, a Sobol-Opposition Initialization, Reference-Vector Dual-Archive Management, and Reinforcement Learning-Regulated Multi-Objective Grey Wolf Optimizer (SORD-RL-MOGWO) is developed. Sobol-opposition initialization enhances initial population diversity and feasible-space coverage, reference-vector dual-archive management balances convergence and distribution uniformity, and reinforcement learning adaptively regulates exploration and exploitation during the search. Under validation conditions of a cutting speed of 20 m/min and a feed rate of 0.060 mm/r, the mechanical performance model achieved coefficients of determination of 0.98 and 0.99 for axial force and cutting torque, with average relative errors of 1.38% and 1.04%, respectively. SORD-RL-MOGWO achieved a hypervolume of 0.78 ± 0.01 and a feasible solution ratio of 95.93 ± 1.72%, outperforming MOGWO, C-TAEA2, CMOEA-TSRA, and DRLOS-EMCMO. Across feed rates of 0.040–0.100 mm/r at 20 m/min, the optimized tool consistently reduced axial force, cutting torque, and chip blockage. At 0.100 mm/r, axial force and cutting torque were reduced by 14.23% and 14.00%, respectively, while the chip blockage rate decreased from 55.0% to 20.0%. These results demonstrate that the proposed method provides a practical approach to reducing cutting loads and chip-evacuation failure while maintaining structural feasibility, thereby improving tool reliability and process stability in the industrial deep-hole trepanning of difficult-to-machine alloys such as GH4169.

1. Introduction

Deep-hole components made from difficult-to-machine alloys are widely used in aero-engine shafts, landing-gear cylinders, nuclear-power equipment, and other safety-critical systems, where machining accuracy, material utilization, and process stability are strictly required. Deep-hole trepanning has considerable application value because it enables hole formation while retaining the central core material. However, the enclosed cutting zone, narrow chip-evacuation path, and strong coupling among tool parameters can increase cutting loads, promote chip blockage, and reduce cutting-edge reliability [1-3]. Therefore, coordinated optimization of deep-hole trepanning

*Corresponding author: gzkgf2008@163.com
[a]orcid.org/0009-0002-7399-0423; [b]orcid.org/0009-0004-5337-4687
DOI: http://dx.doi.org/10.17515/resm2026-1887vk0717rs

tool geometry is necessary to improve machining performance and adaptability under demanding operating conditions. Foundational studies have shown that BTA deep-hole trepanning involves coupled cutting-force generation, chip formation, and guide-pad support. The asymmetric cutting structure governs axial and radial loads, while the guide pads provide self-guiding and burnishing effects that influence bore accuracy and process stability [4-5].

In terms of deep-hole machining mechanism and tool structure, Strodick, S., et al. studied the problem of subsurface control in the deep-hole drilling process of the Boring and Trepanning Association (BTA), analyzed the influence of deep-hole machining conditions on the surface performance and service performance of the workpiece. Moreover, they demonstrated that deep-hole tool structure and machining state not only affected the hole formation process, but also related to the functional reliability of the machined surface [6]. Wegert R et al. further proposed a sensor integrated tool approach for single-edge deep-hole drilling, studying the relationship between process state and surface performance through near-cutting area information acquisition, providing a technical basis for load monitoring and condition regulation in deep-hole machining [7]. The above studies strengthened process-state perception and machining-quality evaluation but mainly focused on surface-performance regulation and process monitoring. Therefore, systematic co-optimization of the primary trepanning-tool variables, including rake angle, clearance angle, point angle, edge radius, chip-breaker width, and chip-groove guide angle, remains insufficiently investigated.

In terms of tool structure influence and drilling performance evaluation, Atif M et al. studied the effect of different tool designs on drilling performance using ultrasonic-assisted drilling of fiber-metal laminas as the object, indicating a close connection between tool geometry and machining load and hole machining quality [8]. Despite the differences in the processing objects and deep-hole trepanning conditions, the study showed that it was feasible to improve the performance of the drilling process through structured design. For deep-hole trepanning, annular cutting structures, closed chip removal channels, and retained mandrel features made the coupling between tool parameters more prominent [9]. This coupling arises because the rake and point angles simultaneously redistribute cutting deformation, axial load, and chip-flow direction, whereas the edge radius, chip-breaker width, and chip-groove guide angle affect both edge strength and chip curling, with excessive strengthening or flow restriction potentially increasing friction, torque, and chip congestion. Therefore, relying solely on empirical selection or single-objective optimization makes it difficult to obtain a parameter scheme that simultaneously ensures low cutting loads, low chip-blockage risk, and structural safety.

Constrained multi-objective evolutionary algorithms provide an effective approach to complex mechanical parameter optimization. Qiao K et al. emphasized the balance among convergence, solution distribution, and constraint satisfaction [10], which is consistent with the coupled constraints of edge thickness, structural safety, and chip-evacuation area in deep-hole trepanning tool design. Ming F et al. introduced deep reinforcement learning for adaptive operator selection under complex constraints [11], while Zheng J incorporated Q-learning into Multi-objective Grey Wolf Optimizer (MOGWO) to dynamically switch search strategies and improve multi-objective optimization performance [12]. However, general-purpose MOGWO methods are not well suited to deep-hole trepanning geometry optimization because the coupled structural and chip-evacuation constraints create a narrow and discontinuous feasible region. Conventional population initialization and leader selection may generate excessive infeasible solutions, concentrate individuals around a few dominant solutions, and cause premature convergence and diversity loss, thereby limiting the coverage of feasible Pareto-optimal designs. In deep-hole trepanning, the retained central core narrows the annular chip-evacuation space, increases the confinement of chip curling and transport, and strengthens the coupling between chip-control geometry, cutting load, and blockage risk. However, this core-induced constraint has not been adequately considered in existing tool-geometry optimization studies.

In summary, previous studies have not provided a unified framework for the constrained multi-objective geometry optimization of deep-hole trepanning tools. To address this gap, a coupled evaluation model of axial force, cutting torque, and chip-evacuation risk is established, and a Sobol-

Opposition Initialization, Reference-Vector Dual-Archive Management, and Reinforcement Learning-Regulated Multi-Objective Grey Wolf Optimizer (SORD-RL-MOGWO) is developed. The MOGWO provides the Pareto-search framework for balancing conflicting performance objectives. Sobol-opposition initialization improves population coverage within the narrow feasible region, while reference-vector dual-archive management prevents solution aggregation and maintains convergence and diversity. Reinforcement learning dynamically selects search strategies according to the population state, thereby reducing premature convergence and balancing exploration and exploitation. The resulting framework generates structurally feasible Pareto-optimal geometries under multiple feed conditions.

2. Methods and Materials

2.1. Research Framework

During the deep-hole trepanning process, the enclosed cutting zone and restricted chip evacuation make tool performance highly sensitive to geometric parameters, potentially increasing axial force and torque, destabilizing chip breaking, and weakening edge load capacity [13–14]. Therefore, a parameter-optimization method combining mechanical-performance evaluation with an improved MOGWO is developed to coordinate cutting load, chip evacuation, and structural reliability. The research framework for the multi-objective geometric optimization of deep-hole trepanning tools is shown in Figure 1.

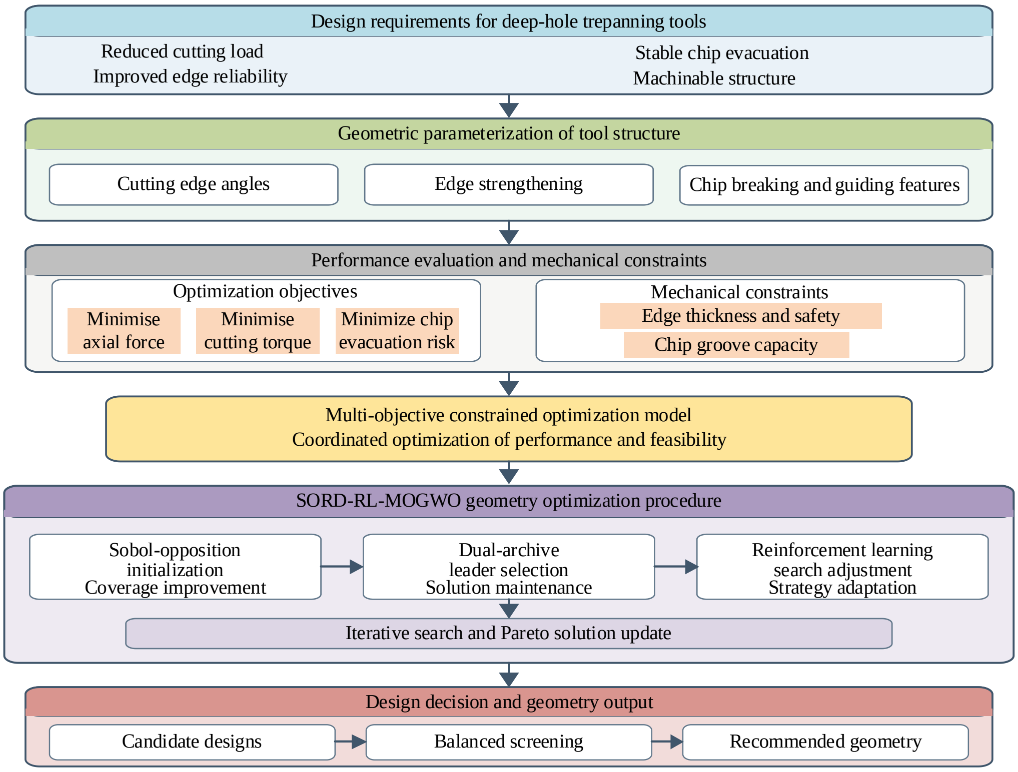

Fig. 1. Research technology roadmap

Figure 1 illustrates the overall research framework. First, the key geometric parameters affecting cutting load, edge reliability, and chip-evacuation stability are identified and defined as bounded design variables. Under consistent workpiece, tool-material, and cutting conditions, axial force, cutting torque, and chip-evacuation risk are jointly evaluated to establish a constrained multi-objective optimization model that also considers structural safety and chip-channel capacity. During optimization, Sobol–opposition initialization improves design-space coverage, the reference-vector dual-archive mechanism balances convergence and solution distribution, and reinforcement learning dynamically selects the grey wolf search strategy. Finally, Pareto-optimal parameter combinations satisfying low cutting load, low chip-evacuation risk, and structural-safety requirements are screened to obtain the optimized deep-hole trepanning tool design.

In Figure 1, the design requirements represent system-level performance targets rather than direct constraint equations. Reduced cutting load is expressed through the axial-force and cutting-torque objectives, while stable chip evacuation is represented by the chip-evacuation-risk objective and the minimum chip-groove area. Edge reliability and structural manufacturability are ensured through the minimum effective edge thickness, structural safety margin, and variable bounds. Therefore, the mechanical constraints define the feasible design region within which the performance objectives are optimized.

2.2. Materials, Tool Configuration, and Experimental Setup

Physical cutting tests were designed to evaluate the applicability of SORD-RL-MOGWO to the geometric optimization of deep-hole trepanning tools. The workpiece material was aged GH4169 bar stock, and an indexable carbide trepanning tool with an outer diameter of 32 mm, a retained-core diameter of 18 mm, and an effective machining depth of 100 mm was used. Because GH4169 retains high strength at elevated temperatures and has low thermal diffusivity, heat tends to accumulate near the tool–chip interface during enclosed deep-hole machining, thereby changing the material flow stress, friction state, contact length, axial force, and cutting torque. High-pressure internal coolant also generates additional axial thrust and a smaller torque component. These thermal and hydraulic effects were considered to avoid incorrectly attributing condition-dependent loads to tool geometry. Coolant pressure, flow rate, and cutting speed were therefore kept constant in all tests. Axial force and cutting torque were synchronously collected at a sampling frequency of 10 kHz. The stable cutting signals were low-pass filtered, and their mean values were used for subsequent analysis. The main material properties and experimental conditions are listed in Table 1.

Table 1. Experimental and platform, processing conditions settings

Category	Item	Setting
Workpiece Conditions	Verification material	GH4169 aged bar
	Material hardness	42.6 ± 0.7 HRC
	Blank dimensions	Diameter 52 mm × Length 160 mm
Tool Conditions	Tool structure	Indexable deep-hole trepanning tool
	Insert material and coating	Carbide inserts, TiAlN coating
	Trepanning outer diameter / Core diameter	32 mm / 18 mm
Cutting Conditions	Cutting speed	20 m/min
	Feed rate	0.040, 0.060, 0.080, 0.100 mm/rev
	Machining depth	100 mm
	Cooling method	High-pressure internal coolant
	Coolant pressure	4.0 MPa
	Coolant flow rate	18 L/min
Measurement Conditions	Axial force range	0–5 kN
	Axial force measurement accuracy	±0.2% full scale, ±10 N
	Torque range	0–50 N·m
	Torque measurement accuracy	±0.2% full scale, ±0.10 N·m
	Sampling frequency	10 kHz
Repetition Settings	Number of load test repetitions	5 times per condition
	Number of chip clogging observation trials	20 times per condition

The coolant pressure of 4.0 MPa and flow rate of 18 L/min were selected based on preliminary cutting tests and the stable operating range of the cooling system. Lower settings resulted in intermittent chip retention at a machining depth of 100 mm, whereas further increases provided no clear improvement in chip evacuation and increased hydraulic disturbance. Therefore, these values were adopted to balance chip-evacuation stability and load-measurement reliability. The 10 kHz sampling rate was used to capture the original force and torque signals and identify unstable cutting segments. However, the optimization focused on quasi-steady cutting performance; therefore, tool-entry transients and chatter-related fluctuations were excluded, and the low-pass-filtered mean values from the stable cutting stage were used as the evaluation responses. Dynamic stability indicators were not included as independent optimization objectives.

Chip blockage was evaluated through 20 independent cutting trials for each tool geometry and feed-rate condition. A trial was classified as blocked when accumulated chips visibly obstructed the annular evacuation channel and required feed interruption or manual chip removal. Transient torque fluctuations without visible channel obstruction were not counted as blockage. The chip-blockage rate was calculated as the number of blocked trials divided by 20.

2.3. Geometric Parametric Design of Deep-Hole Trepanning Tools and Multi-Objective Optimization Model

Recent research on BTA deep-hole machining of GH4169 has shown that tool structure and material selection significantly affect cutting performance and hole quality [15]. Therefore, the cutting region and chip-guiding region were parameterized to provide the design variables for subsequent multi-objective optimization. The structure diagram of the key geometric parameters of the deep-hole trepanning tool is shown in Figure 2.

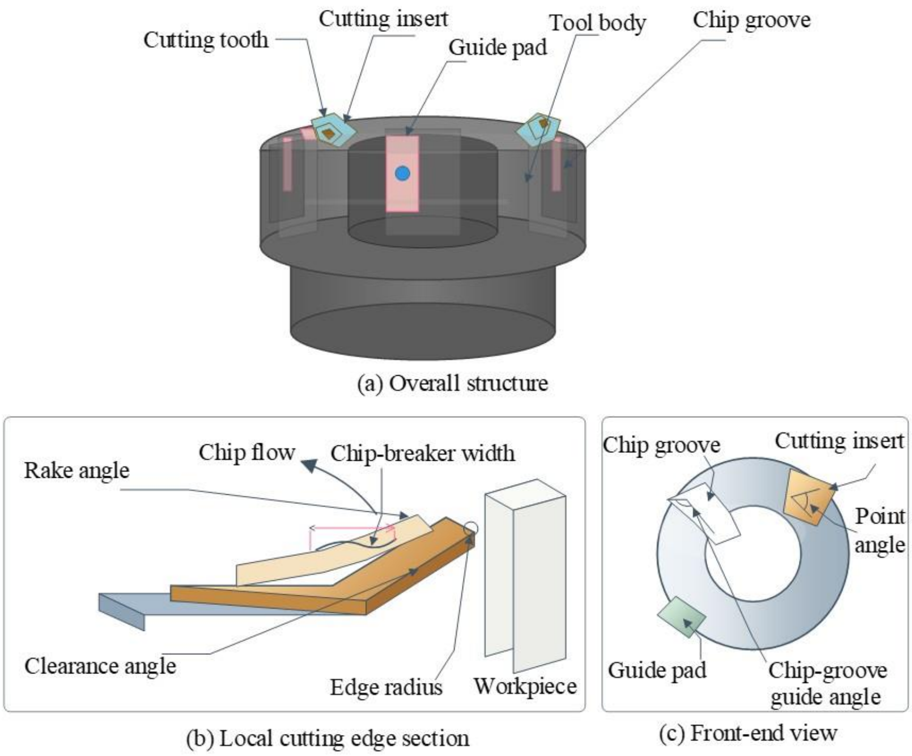

Fig. 2. Schematic diagram of the key geometric parameters and structure of the deep-hole trepanning tool

In Figure 2, the rake angle regulates material flow along the rake face and cutting resistance, while the clearance angle affects flank–workpiece contact and cutting-edge support. The point angle redistributes the cutting load, and the edge radius balances cutting sharpness and resistance to chipping. The width of the chip breaking table regulates the bending and breaking state of the chips. The chip-groove guide angle defines the preferred chip-flow direction and alters the effective chip-evacuation channel area. This design function is consistent with established findings that chip-channel geometry affects chip transport, coolant flow, and tool stiffness in deep-hole drilling [16-17]. This system of geometric parameters can systematically characterize the combined effect of tool structure on cutting performance and chip removal efficiency. Thus, the study defines the geometric design variables of deep-hole trepanning tools as shown in Equation (1).

$$\boldsymbol{x} = [\gamma, \alpha, \varphi, r_e, b_c, \theta_g]^T, \quad \boldsymbol{x}^L \leq \boldsymbol{x} \leq \boldsymbol{x}^U \tag{1}$$

In Equation (1), $\mathbf{x}$ represents the tool geometric parameter vector. γrepresents the rake angle. αrepresents the clearance angle. φ represents the point angle. r_e indicates the radius of the edge arc. b_c indicates the width of the chip breaking table. θ_g represents the chip-groove guide angle. $\mathbf{x}^L$and $\mathbf{x}^U$ represent the lower limit vector and upper limit vector of the allowable values for each design variable. Superscript T indicates matrix transposition. The physical limits used in the optimization are listed in Table 2.

Table 2. Physical limits of the geometric design variables

Variable	Physical meaning	Unit	Lower limit	Upper limit
γ	Rake angle	°	6.0	18.0
α	Clearance angle	°	5.0	12.0
φ	Point angle	°	110.0	125.0
r_e	Edge radius	mm	0.1	0.3
b_c	Chip-breaker width	mm	0.8	1.6
θ_g	Chip-groove guide angle	°	15.0	35.0

Accordingly, the lower- and upper-bound vectors were defined as $\mathrm{x}^L = [6.0,5.0,110.0,0.10,0.80,15.0]^{\mathrm{T}}$ and $\mathrm{x}^U = [18.0,12.0,125.0,0.30,1.60,35.0]^{\mathrm{T}}$, respectively. These bounds restrict the search to geometrically feasible and manufacturable tool configurations. Tool geometry affects machining performance through coupled mechanisms: cutting-edge angles govern load generation, the edge radius influences structural capacity, and chip-breaker and chip-groove parameters control chip flow and blockage risk [18]. Their relationships with the multi-objective responses are shown in Figure 3.

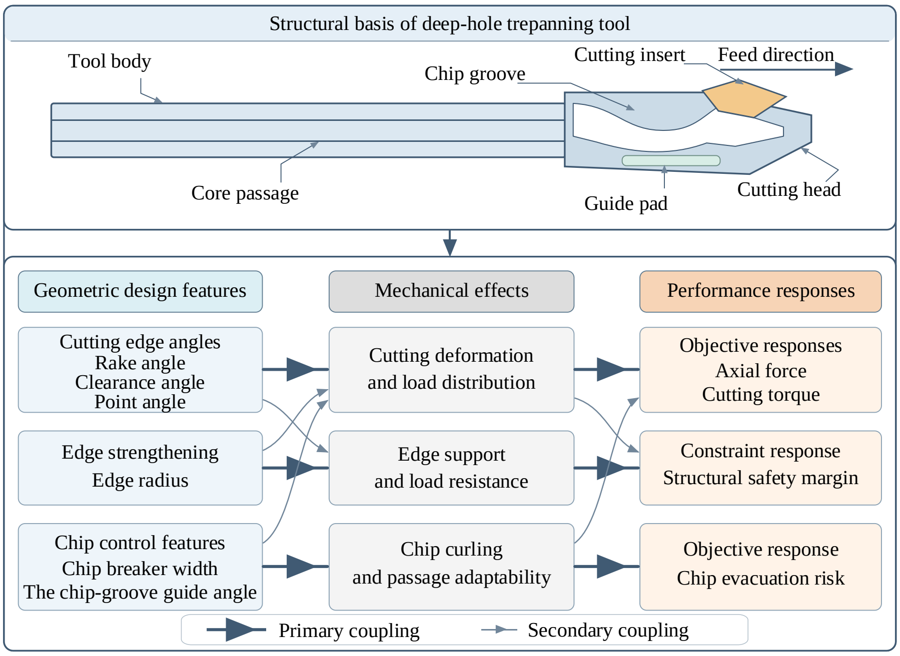

Fig. 3. Relationship diagram between tool geometric parameters and multi-objective performance responses

Under the conditions of fixed cutting speed, feed rate and processing material, the study divides the annular cutting edge of the trepanning tool into N micro-element cutting edge segments and calculates the axial force and tangential force contributions generated by each micro-element cutting edge segment based on the mechanical cutting coefficient. Unlike a conventional drill, the indexable trepanning tool has an annular cutting edge constrained by the retained core. Along this edge, the radial position, local cutting speed, undeformed cutting area, effective engaged length, and torque arm vary continuously. Therefore, the cutting edge is divided into N micro-element segments, within each of which the local geometry and cutting coefficients are assumed to be approximately uniform. The axial-force and tangential-force contributions of all segments are then summed, while the torque contribution is weighted by the corresponding radial distance, as expressed in Equation (2).

$$\begin{cases} F_z(\boldsymbol{x}) = \sum_{j=1}^{N} \left[K_{zc,j}(\boldsymbol{x})A_j + K_{ze,j}(\boldsymbol{x})l_j\right] \\ M_t(\boldsymbol{x}) = \sum_{j=1}^{N} r_j \left[K_{tc,j}(\boldsymbol{x})A_j + K_{te,j}(\boldsymbol{x})l_j\right] \end{cases} \tag{2}$$

In Equation (2), $F_z(\mathbf{x})$ represents the evaluation value of the overall axial force of the tool. $M_t(\mathbf{x})$ represents the overall cutting torque evaluation of the tool. j represents the micro-element number of the cutting edge. N represents the total number of micro-elements. A_j represents the jth undeformed cutting area corresponding to the cutting-edge segment. l_j represents the jth effective cutting-edge length of the cutting-edge segment. r_j indicates the radial distance from the cutting edge to the center of rotation of the tool. $K_{zc,j}$ $K_{zc,j}$ and $K_{ze,j}$ represent the j th axial shear load coefficient and the axial edge load coefficient of the cutting-edge section. $K_{tc,j}$And $K_{te,j}$ represent the tangential shear load coefficient and the tangential edge load coefficient.

Under the fixed workpiece, feed, spindle-speed, and coolant conditions, the cutting coefficients were assumed to remain constant along the insert. Although the local cutting speed increases with radial position, its variation within the narrow annular cutting range was limited. The resulting torque difference was represented through the local undeformed cutting area, effective cutting-edge length, and radial torque arm of each micro-element. Any residual influence of cutting-speed variation was implicitly included in the experimentally calibrated coefficients. Therefore, the model is applicable to the tested cutting-speed range, whereas a wider speed range would require speed-dependent coefficient calibration.

GH4169 work hardening increases local flow stress, particularly at smaller edge radii. Since the micro-elements represent simultaneously engaged edge segments, they do not successively cut the same hardened layer. The average work-hardening effect was therefore incorporated into the experimentally calibrated cutting coefficients. The cutting coefficients were identified experimentally using 18 tool-geometry schemes. The geometric terms and stable-stage measured loads were fitted by least squares to determine the axial and tangential shear and edge coefficients. All calibration tests were conducted on GH4169 at 20 m/min and 0.060 mm/r under fixed coolant conditions, and the identified coefficients were kept unchanged during validation and optimization.

Considering the characteristics of long chip removal paths and limited channel space in deep-hole machining, the study further constructs the chip removal risk assessment function based on the chip curling state and the matching relationship of the chip removal channel, as shown in Equation (3).

$$R_c(\boldsymbol{x}) = \lambda_1 \frac{R_\chi(\boldsymbol{x})}{R_{lim}} + \lambda_2 \frac{A_\chi(\boldsymbol{x})}{A_g(\boldsymbol{x})} + \lambda_3 \frac{L_\chi(\boldsymbol{x})}{L_{lim}}, \quad \lambda_1 + \lambda_2 + \lambda_3 = 1 \tag{3}$$

In Equation (3), $R_c(\mathbf{x})$ represents the risk assessment value for chip removal. $R_\chi(\mathbf{x})$ represents the chip curling radius determined by the chip breaker structure. R_{lim} represents the maximum allowable chip curling radius. $A_\chi(\mathbf{x})$ represents the equivalent occupied area of chips in the direction of chip discharge. $A_g(\mathbf{x})$ represents the effective channel area of the chip removal groove. $L_\chi(\mathbf{x})$ represents the evaluation value of chip continuous length. L_{lim} represents the maximum allowed continuous chip length. λ_1, λ_2 and λ_3 represent the weight coefficients of the three chip removal evaluation items, all of which are non-negative. The three terms were normalized before aggregation. Equal weights were adopted, with $\lambda_1 = \lambda_2 = \lambda_3 = 1/3$, to avoid subjective preference among chip curling radius, occupied channel area, and continuous chip length. These weights were kept fixed throughout the optimization. The maximum allowable continuous chip length was defined as a condition-specific empirical threshold rather than a universal material constant. It was determined from preliminary chip-morphology observations by identifying the transition from regularly broken chips to long continuous chips associated with unstable evacuation. Because the work-hardening behavior of GH4169 affects chip stiffness and fracture, this threshold is applicable only within the tested tool-geometry, feed-rate, and coolant ranges and should be recalibrated under substantially different machining conditions.

Equation (3) is a reduced-order geometric risk function established under fixed coolant conditions. The coolant pressure and flow rate were maintained at 4.0 MPa and 18 L/min for all calibration, validation, and optimization tests. Therefore, the hydraulic effects on chip curling and transport were implicitly incorporated into the experimentally observed chip behavior, but were not independently identified as model variables. The chip-groove guide angle may alter local flow separation, coolant return velocity, and turbulence intensity, thereby affecting the chip curling radius and evacuation stability. Because coolant velocity and pressure distributions were not measured, introducing an explicit hydraulic term would lack sufficient experimental support. Consequently, the current chip-risk model is valid within the specified coolant conditions and geometric ranges, but its predictive accuracy may decrease when coolant parameters or the chip-groove guide angle vary substantially. Future work will couple coolant-flow measurements or computational fluid dynamics analysis with the chip-risk model to quantify these hydraulic effects.

The retained core further narrows the annular coolant-return and chip-evacuation passage, producing a Venturi-like flow acceleration and an associated pressure gradient. Local contraction, chip accumulation, and flow losses may generate back pressure and additional fluctuations in the measured axial force. Under the fixed retained-core diameter, coolant pressure, and flow rate used in this study, these hydraulic effects were implicitly included in the experimentally calibrated axial-force response. However, the optimization model uses the stable-stage mean axial force and does not treat pressure-induced force fluctuations as an independent objective. Therefore, the current model is applicable to the specified core geometry and coolant conditions, while substantial changes in the annular clearance may require coupled fluid–structure modelling and dynamic pressure measurements.

Based on this, the study aims to minimize axial force, cutting torque, and chip removal risk as optimization objectives. Then, the study uses effective blade thickness, structural safety margin, and chip removal channel area as mechanical design constraints to establish a multi-objective optimization model for the geometric parameters of deep-hole trepanning tools, as shown in Equation (4). Accordingly, the design requirements are converted into performance objectives, whereas the mechanical constraints are imposed as mandatory feasibility conditions for every candidate geometry.

$$\begin{cases} min_{\boldsymbol{x}}\, \boldsymbol{F}(\boldsymbol{x}) = [F_z(\boldsymbol{x}), M_t(\boldsymbol{x}), R_c(\boldsymbol{x})]^T \\ \qquad \boldsymbol{x}^L \le \boldsymbol{x} \le \boldsymbol{x}^U \\ \qquad t_e(\boldsymbol{x}) \ge t_{min} \\ \qquad S_s(\boldsymbol{x}) \ge S_{min} \\ \qquad A_g(\boldsymbol{x}) \ge A_{min} \end{cases} \tag{4}$$

In Equation (4), $\min_{\mathbf{x}} \mathbf{F}(\mathbf{x})$ represents the multi-objective function vector. $t_e(\mathbf{x})$ represents the effective blade thickness. $t_{\min}$ represents the minimum allowable effective blade thickness. $S_s(\mathbf{x})$ represents the safety margin of the tool structure. $S_{\min}$ represents the minimum safety margin requirement. $A_{\min}$ represents the minimum chip removal channel area that ensures chip passage.

The constraint values were calculated from the parameterized tool model. The effective edge thickness was defined as the minimum distance between the rounded cutting edge and the insert-support boundary, and was jointly determined by the rake angle, clearance angle, point angle, and edge radius. The structural safety margin was calculated from the allowable stress and the maximum equivalent stress produced by the predicted axial force and cutting torque. The effective chip-groove area was defined as the minimum groove cross-sectional area projected normal to the chip-flow direction, and was mainly controlled by the chip-breaker width and chip-groove guide angle. These quantities were automatically updated for each candidate geometry before feasibility screening.

A separate thermal objective or constraint was not introduced because the present study focuses on initial tool-geometry optimization under fixed thermal boundary conditions. The cutting speed, coolant pressure, and coolant flow rate were maintained at 20 m/min, 4.0 MPa, and 18 L/min, respectively, so that the thermal state remained comparable among candidate geometries. The influence of heat accumulation on material flow stress, friction, and retained-core clearance was therefore indirectly reflected in the experimentally calibrated axial-force and cutting-torque responses. However, temperature fields and thermally induced deformation were not measured independently, and introducing an explicit thermal constraint without such data would lack experimental support. Future work will incorporate temperature sensing and thermo-mechanical modelling to evaluate thermal expansion and tool–core clearance under higher-load conditions.

2.4. Geometric Parameter Optimization Algorithm Design Based on SORD-RL-MOGWO

In response to the problems of insufficient initial population coverage, easy aggregation of non-dominated solutions and weak adaptability of search strategies in multi-objective optimization of deep-hole trepanning tools, the SORD-RL-MOGWO algorithm is proposed based on the traditional multi-objective grey wolf optimization algorithm. The Sobol-oppositional learning initialization, the leader wolf selection mechanism based on the reference vector double archive, and the reinforcement learning search adjustment mechanism are integrated. To improve initial population coverage, Sobol low-discrepancy sequences are mapped onto the bounded geometric design space [19], while opposition-based learning generates complementary candidates around the center of each parameter interval [20]. The combined initialization mechanism is shown in Figure 4. In Figure 4, the algorithm first maps the Sobol sequence to the actual parameter space based on the upper and lower limits of each geometric parameter of the tool, and then expands the initial candidate schemes through opposition learning. The initialization process is shown in Equation (5).

$$\begin{cases} \boldsymbol{x}_i^0 = \boldsymbol{x}^L + \boldsymbol{s}^i \odot (\boldsymbol{x}^U - \boldsymbol{x}^L) \\ \boldsymbol{x}_i^{op} = \boldsymbol{x}^L + \boldsymbol{x}^U - \boldsymbol{x}_i^0 \end{cases} \tag{5}$$

In equation (5), $\mathbf{x}_i^0$ represents the ith Sobol initial individual. $\mathbf{s}^i$ represents the ith Sobol low difference sampling vector, with each component value located in the [0,1] interval. $\odot$ denotes the Hadamard product, in which each component of the Sobol vector is multiplied by the corresponding component of the tool-parameter range vector. It is an element-wise multiplication operator rather than an additional model parameter. $\mathbf{x}_i^{\mathrm{op}}$ represents the opposing solution of the ith individual. The physical outcome of the opposition mapping is a complementary distribution of the original and opposition candidates around the midpoint of each parameter interval. After feasibility screening, the retained candidates provide broader coverage of the allowable geometric space, particularly near parameter boundaries and sparsely sampled regions. After merging two types of individuals, the algorithm performs initial population screening based on the degree of constraint satisfaction and non-dominated level, thereby enhancing the search coverage ability of different tool structure regions in the initial stage.

To balance the convergence quality and distribution uniformity of the Pareto-optimal tool designs, a reference-vector-based dual-archive leader wolf selection mechanism is introduced. Non-dominated candidate solutions are first associated with different reference-vector regions. The convergence archive preferentially retains solutions close to the ideal objective region, whereas the diversity archive preserves representative solutions from sparsely populated reference directions. During leader selection, the primary leader wolf is selected from the convergence archive, while the other two leader wolves are selected from different sparse regions of the diversity archive [21–22]. This mechanism coordinates convergence and solution-space coverage while preventing excessive concentration of candidate geometries, as shown in Figure 5.

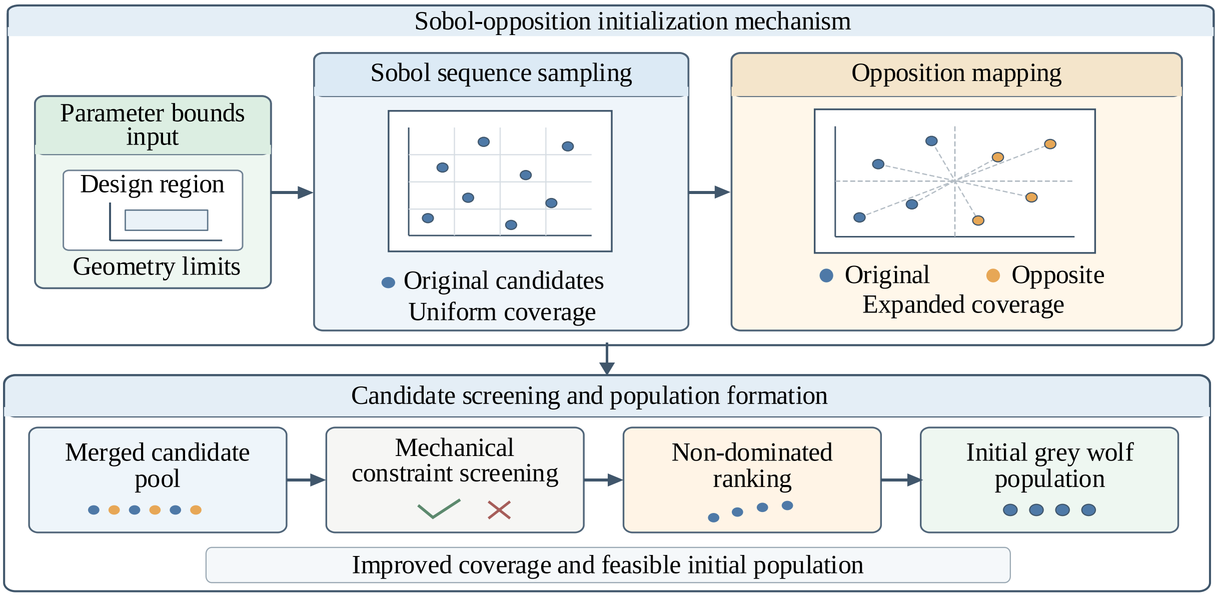

Fig. 4. Sobol–opposition learning initialization mechanism diagram

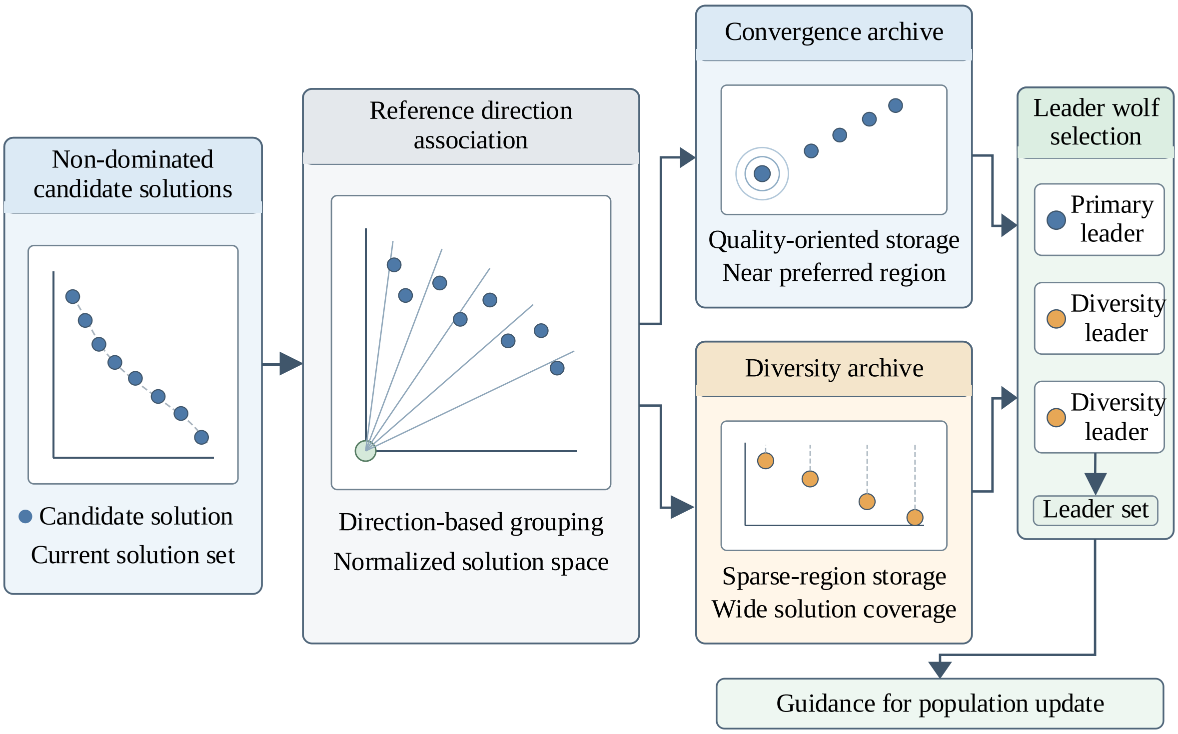

Fig. 5. Reference-vector dual-archive leader-selection mechanism

The probability of the qth reference area being selected as the diversity leadership area is defined as shown in equation (6).

$$p_q = \frac{(n_q + \varepsilon)^{-1}}{\sum_{m=1}^{N_r}(n_m + \varepsilon)^{-1}} \quad (6)$$

In equation (6), p_q represents the probability of selecting the qth reference region. n_q represents the number of schemes associated with the qth reference vector in the diversity archive. N_r represents total number of reference vectors. m represents the reference vector region index. ε is a small positive constant set to 10^{-12} to prevent division by zero when a reference-vector region contains no associated solutions. It was fixed throughout all optimization experiments and has a negligible influence on the selection probabilities of non-empty regions. Regions with fewer options have a higher probability of selection, which can avoid excessive concentration of the solution set. When selecting the leader wolf, α wolf selects from the convergence profile, while β wolf and δ wolf select from different reference areas in the diversity profile to jointly guide the search of the gray wolf population. The preference for sparsely populated reference-vector regions does not imply unstable preservation of extreme solutions. Candidate solutions are associated with reference vectors in the normalized three-objective space, and boundary sectors corresponding to low axial force, low cutting torque, or low chip-evacuation risk generally remain sparsely occupied. These sectors therefore receive higher selection probabilities from the diversity archive, whereas the convergence archive prevents poorly converged boundary solutions from dominating leader selection. Selecting leader wolves from different reference-vector regions consequently preserves extreme solutions while reducing excessive concentration around a single compromise region.

Based on this, the study uses Q-learning to adapt the grey wolf search strategy, dividing the search process into three states: exploration, balance, and exploitation, and configuring corresponding position update actions. The exploratory action focuses on expanding the range of tool parameter search, the balanced action takes into account scheme expansion and target approximation, and the exploitation-oriented action strengthens the guidance of the superior leader wolf to the adjacent area. The search state was updated at the beginning of each iteration according to the normalized iteration progress. The exploration state was assigned during the first 30% of iterations, the balance state during 30%–70%, and the exploitation state during the final 30%. If the hypervolume did not improve for five consecutive iterations, the state was temporarily reset to exploration to avoid search stagnation. These transition criteria were fixed for all optimization runs. The SORD-RL-MOGWO algorithm process is shown in Figure 6.

In Figure 6, SORD-RL-MOGWO generates initial populations through Sobol-opposition learning, calculates axial force, cutting torque, and chip removal risk for each tool scheme, and screens out infeasible individuals based on mechanical constraints. During the iteration, the reference vector double file mechanism is used to update the non-dominated scheme and select the leader wolf, while the reinforcement learning module adaptively selects the position to update the action based on the search state. To measure the contribution of different actions to the optimization process, the study constructs a reward function by combining the degree of improvement in the Pareto solution set, the number of new feasible non-dominated schemes, and the degree of constraint violation. Moreover, the study uses Q-learning to update the action value, as shown in Equation (7).

$$\begin{cases} r_t = \eta_1 \Delta HV_t + \eta_2 \Delta N_t - \eta_2 V_t \\ Q_{t+1}(s_t, a_t) = Q_t(a_t, a_t) + \rho \left[r_t + t \max_{a \in A} Q_t(s_{t+1}, a) - Q_t(s_t, a_t) \right] \end{cases} \tag{7}$$

In equation (7), r_t represents the reward value obtained in the tth iteration. ΔHV_t represents the increment of the Pareto solution set hypervolume in this iteration. ΔN_t represents the number of feasible non dominated tool options added. V_t represents the degree of violation of population constraints. η_1, η_2 and η_2 represent reward evaluation weights. $Q_t(s_t, a_t)$ represents the value of selecting action a_t in state a_t during the tth iteration. ρ represents the learning rate. t represents the discount factor. A represents the set of search actions. a represents candidate actions in the action set. s_{t+1} represents the next iteration state. All reward terms were normalized before aggregation. The weights η_1, η_2 and η_2 were set to 0.4, 0.3, and 0.3, respectively, through preliminary grid-search experiments, giving greater emphasis to Pareto-set improvement while balancing feasible-solution generation and constraint control. The learning rate ρ was set to 0.2. The discount factor ζ was set to 0.9 to retain long-term search feedback without excessively weakening the influence of the current reward. These parameters were fixed in all experiments.

Exploration does not rely on unrestricted random action selection. An ε-greedy policy was adopted, with ε set to 0.30, 0.15, and 0.05 during the exploration, balance, and exploitation stages, respectively. Therefore, most actions are selected according to the current Q-values, while limited randomness is retained to avoid premature convergence. The reward is evaluated at the end of each iteration, and the Q-table is updated immediately with a learning rate of 0.20; consequently, the search strategy can change in the next iteration. A discount factor of 0.90 propagates delayed improvements to previous state–action pairs. If the hypervolume does not improve for five consecutive iterations, the search state is temporarily returned to exploration. The hypervolume reward jointly reflects convergence towards the Pareto front and objective-space coverage.

However, the reinforcement learning module does not independently determine solution uniformity. Distribution homogeneity and boundary-solution preservation are primarily maintained by the reference-vector dual-archive mechanism. The reinforcement learning module adjusts the search strategy according to hypervolume improvement, feasible-solution generation, and constraint satisfaction, thereby promoting promising regions without concentrating the population exclusively around the knee point.

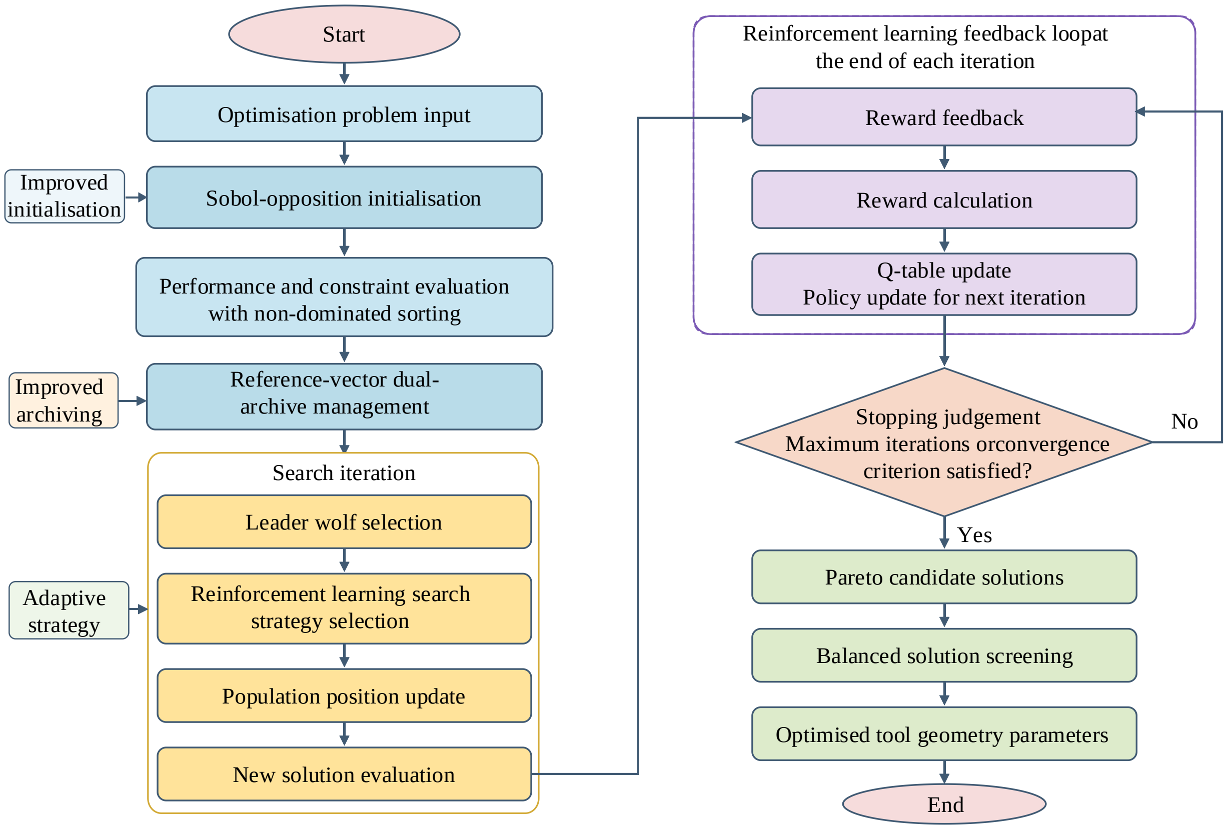

Fig. 6. Flowchart of the SORD-RL-MOGWO algorithm

After reaching the termination condition, the algorithm outputs a Pareto scheme set that satisfies mechanical constraints, and normalizes the evaluation of axial force, cutting torque, and chip removal risk. Combined with structural safety margin, a knee point scheme with comprehensive performance coordination is selected. Finally, the rake angle, clearance angle, point angle, edge radius, chip-breaker width, and chip-groove guide angle are determined.

3. Results

3.1. Practical Cutting Verification of The Mechanical Performance Evaluation Model

The cutting coefficients were calibrated using the 18 tool-geometry schemes described in Section 2.3. Eight additional schemes that were not involved in coefficient identification were used for independent validation. They covered both interior regions and parameter combinations near the allowable boundaries rather than being concentrated in a narrow safe region. All validation tests were conducted under the same machining conditions, and the model validity is therefore limited to the specified geometric ranges and cutting conditions. The calibrated coefficients were fixed throughout the validation process, and the predicted axial force and cutting torque were compared with the stable-stage measured values, as shown in Figure 7.

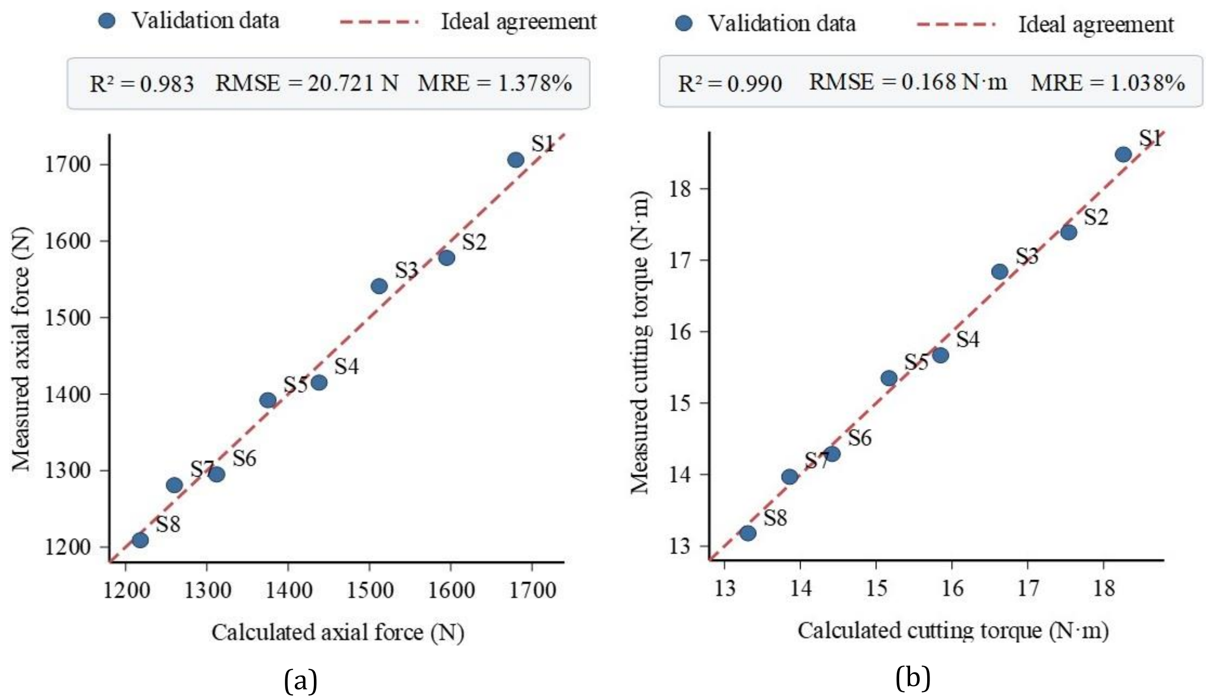

Fig. 7. Actual cutting verification results of the mechanical properties evaluation model (a) Axial force verification and (b) Cutting torque verification

In Figure 7 (a), the calculated values of the axial force were generally close to the ideal line of conformity with the verified values. The coefficient of determination, root mean square error, and mean relative error were 0.983, 20.721 N, and 1.378%, indicating that the model could well reflect the influence of changes in tool geometry parameters on the axial cutting load. In Figure 7 (b), the calculated value of the cutting torque was also highly consistent with the verified value, with a coefficient of determination of 0.990, root mean square error and average relative error of 0.168 N·m and 1.038%. It indicated that the model had a high predictive accuracy for torsional load changes. To sum up, the established mechanical performance evaluation model had good engineering reliability and could provide an effective basis for the subsequent multi-objective optimization of tool geometry parameters. The agreement obtained for both interior and near-boundary schemes indicates that the model maintains satisfactory prediction accuracy across the feasible parameter space.

3.2. SORD-RL-MOGWO Sensitivity Analysis of Key Parameters

To evaluate the influence of key parameter settings on optimization performance, sensitivity experiments were conducted using the algorithm configuration summarized in Table 3.

Table 3. Algorithm settings

Category	Item	Setting
Algorithm Settings	Population size	100
	Maximum function evaluations	10,000
	Number of independent runs	30
	Dual-archive capacity	150
	Reinforcement learning rate	0.2

In SORD-RL-MOGWO, the dual-archive capacity affects objective-space coverage, while the learning rate influences search stability. The tested ranges were determined through preliminary optimization trials and the scale of the current problem. Dual-archive capacities of 50–250 were selected at intervals of 50 to cover undersized, moderate, and relatively large archives with respect to the population size of 100. Capacities below 50 caused frequent deletion of non-dominated solutions, whereas capacities above 250 produced little improvement in Pareto-front coverage but increased archive-management cost. Learning rates from 0.05 to 0.40 were examined to represent conservative to relatively rapid Q-value updates. Values below 0.05 resulted in slow strategy adaptation, while values above 0.40 caused noticeable oscillations in action selection during preliminary tests. Sensitivity and convergence analyses were conducted over 30 independent runs, as shown in Figure 8.

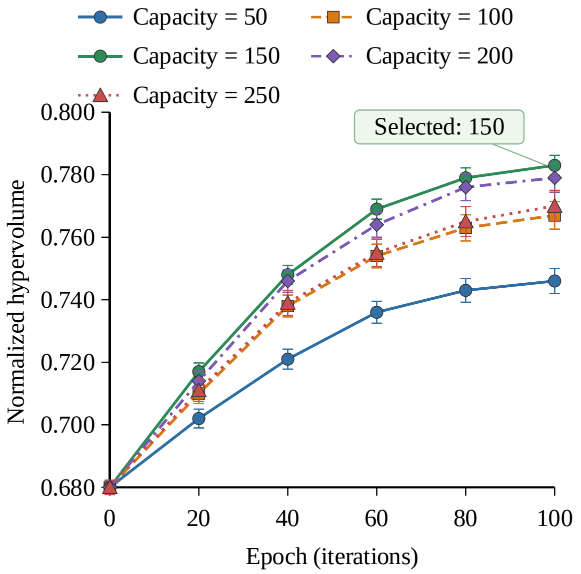

(a) Hypervolume convergence under different dual-archive capacities

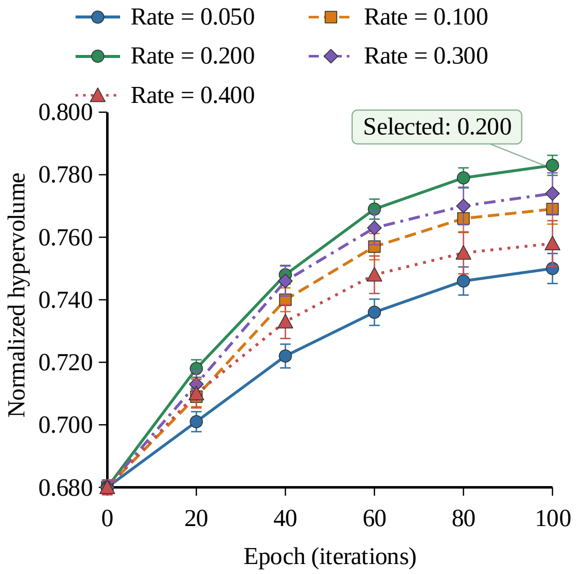

(b) Hypervolume convergence under different learning rates

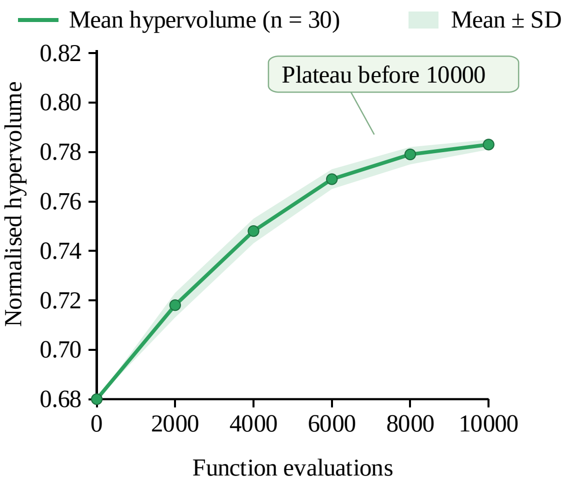

(c) Hypervolume evolution over function evaluations across 30 independent runs

Fig. 8. Results of the sensitivity analysis for key parameters of SORD-RL-MOGWO

Figure 8 presents the sensitivity analysis results of the dual-archive capacity and learning rate. Each data point represents the mean hypervolume over 30 independent runs, and the error bars indicate the corresponding standard deviation. As shown in Figure 8(a), the hypervolume first increases with archive capacity and then tends to stabilize. A capacity of 150 achieves the highest mean hypervolume with relatively small dispersion and is therefore selected. As shown in Figure 8(b), the learning rate of 0.200 yields the best overall performance in terms of both convergence quality and stability. Although higher learning rates such as 0.300 and 0.400 can still improve the hypervolume, their error bars become larger in the middle and later stages of the search, indicating increased run-to-run fluctuation and reduced search stability. Therefore, 0.200 is adopted as the final learning rate. Figure 8(c) presents the mean hypervolume trajectory over 30 independent runs. The curve gradually reached a stable plateau before 10,000 function evaluations, and only limited improvement was observed during the final evaluation stage. Therefore, 10,000 function evaluations were sufficient to balance convergence quality and computational cost for the six-variable optimization problem.

Table 4. Effect of dual-archive capacity on Pareto-front continuity

Archive capacity	Hypervolume	Spacing	Feasible solution ratio/% ↑	Occupied reference-vector regions (%)	Maximum normalized gap ↓	Extreme-solution retention (%)	Runtime (s)
50	0.742 ± 0.021	0.064 ± 0.009	91.82 ± 2.91	66.7 ± 4.8	0.124 ± 0.018	76.7 ± 6.1	18.62 ± 0.48
100	0.772 ± 0.015	0.045 ± 0.006	94.71 ± 2.08	84.1 ± 3.6	0.081 ± 0.011	91.1 ± 3.9	19.54 ± 0.53
150	0.783 ± 0.012	0.036 ± 0.005	95.93 ± 1.72	91.8 ± 2.7	0.059 ± 0.008	97.2 ± 2.1	20.68 ± 0.61
200	0.781 ± 0.013	0.035 ± 0.005	95.86 ± 1.79	92.5 ± 2.5	0.056 ± 0.007	97.9 ± 1.8	22.18 ± 0.70
250	0.779 ± 0.014	0.037 ± 0.006	95.72 ± 1.88	92.9 ± 2.6	0.055 ± 0.008	98.1 ± 1.7	23.86 ± 0.84

To assess whether an archive capacity of 150 is sufficient, five capacities were compared over 30 independent runs using Pareto-front continuity and convergence indicators, as shown in Table 4. Table 4 shows that an archive capacity of 50 is insufficient to maintain Pareto-front continuity, as indicated by a reference-vector occupancy of only 66.7%, a maximum normalized gap of 0.124, and an extreme-solution retention rate of 76.7%. Increasing the capacity to 150 raises the occupancy to 91.8%, reduces the maximum gap to 0.059, and retains 97.2% of the objective-wise extreme solutions. Although capacities of 200 and 250 provide marginal improvements in coverage and extreme-solution retention, their hypervolume does not increase, while runtime rises by 7.3% and 15.4%, respectively, relative to a capacity of 150. Therefore, a capacity of 150 is sufficient to preserve Pareto-front continuity and boundary solutions while maintaining favorable convergence and computational efficiency.

3.3. Comparison of optimization algorithm performance and ablation analysis

The study further introduced three advanced constrained multi-objective optimization methods for comparison: the Constrained Multi-objective Evolutionary Algorithm with an Improved Two-Archive Strategy (C-TAEA2) [23], the Constrained Multi-objective Evolutionary Algorithm with Two-Stage Resource Allocation (CMOEA-TSRA) [24], and the Deep Reinforcement Learning-assisted Operator Selection embedded in Evolutionary Multitasking Constrained Multi-objective Optimization (DRLOS-EMCMO) [25]. The Pareto-optimal solution sets generated by these algorithms were first compared, as shown in Figure 9.

In Figure 9 (a), the Pareto scheme obtained by SORD-RL-MOGWO was overall located on the lower left side of the contrast method. The axial force and cutting torque of its low-torque scheme were 1387 N and 13.180 Nm, which were lower than those of MOGWO, 1470 N and 13.490 Nm, it showed that the improved search mechanism helped to reduce the cutting load. Among the obtained Pareto solutions, the selected low-risk scheme achieved an axial force of 1387 N and a chip-removal risk value of 0.146. The corresponding point is highlighted in Figure 9(b) for visual identification. In Figure 9 (c), the study method achieved a lower chip removal risk with cutting torque close to that of DRLOS-EMCMO, demonstrating a more reasonable performance trade-off. Overall, SORD-RL-MOGWO could generate a set of tool geometry parameter schemes with better distribution and more reasonable compromise relationships.

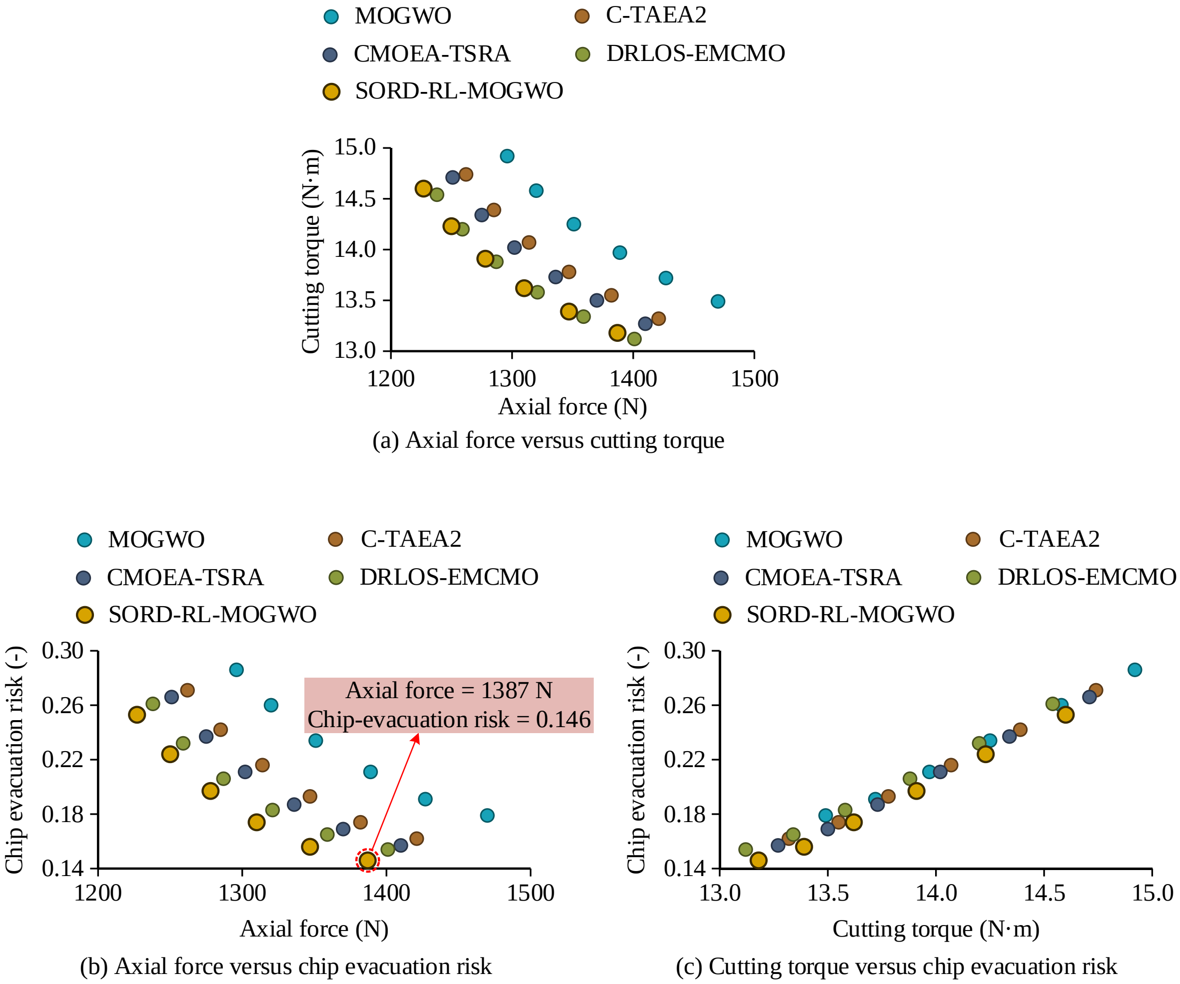

Fig. 9. Distribution of Pareto parameter schemes obtained using different multi-objective optimization algorithms

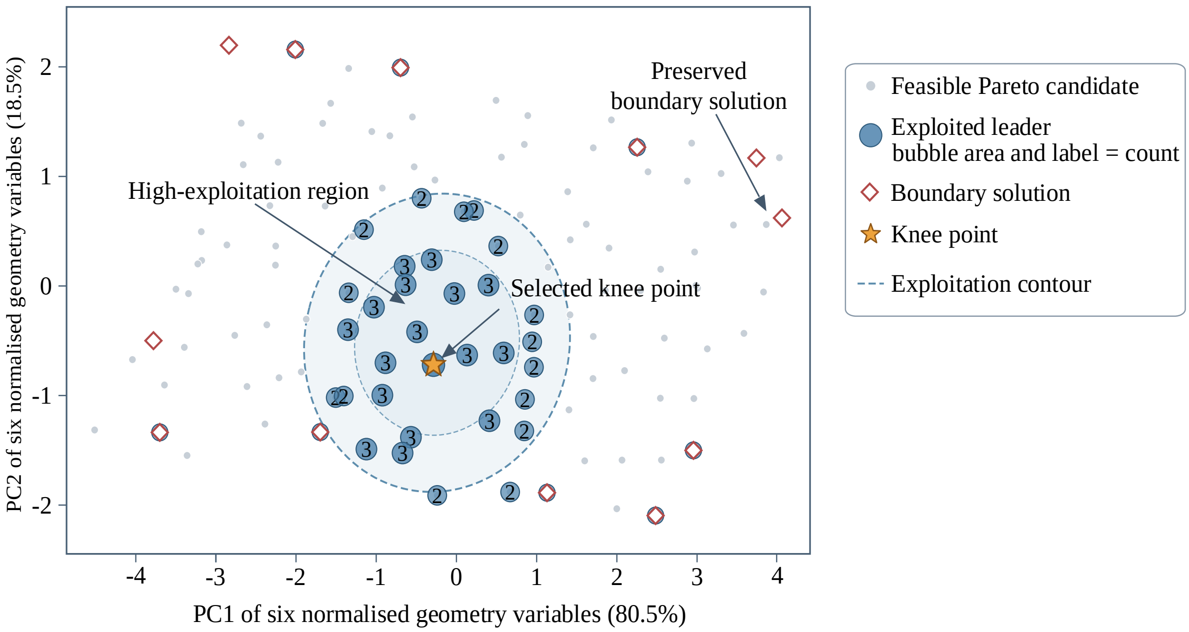

Fig. 10. Exploitation distribution before knee-point selection

Table 5. Performance comparison of different optimizers and ablated configurations of SORD-RL-MOGWO

Method	Hypervolume	Inverted generational distance	Spacing	Feasible solution ratio (%)	Running time (s)
MOGWO	0.689 ± 0.027 $p < 0.001$	0.091 ± 0.013 $p < 0.001$	0.074 ± 0.012 $p < 0.001$	83.73 ± 3.10 $p < 0.001$	14.33 ± 0.85 $p < 0.001$
C-TAEA2	0.754 ± 0.017 $p < 0.001$	0.058 ± 0.008 $p < 0.001$	0.043 ± 0.006 $p < 0.001$	92.27 ± 2.15 $p < 0.001$	19.14 ± 1.02 $p < 0.001$
CMOEA-TSRA	0.760 ± 0.015 $p < 0.001$	0.054 ± 0.007 $p < 0.001$	0.046 ± 0.007 $p < 0.001$	94.03 ± 1.96 $p < 0.001$	18.51 ± 0.96 $p < 0.001$
DRLOS-EMCMO	0.773 ± 0.013 $p = 0.008$	0.050 ± 0.006 $p = 0.039$	0.040 ± 0.006 $p = 0.005$	95.07 ± 1.81 $p = 0.085$	23.73 ± 1.26 $p < 0.001$
SORD-RL-MOGWO	0.783 ± 0.012 —	0.047 ± 0.006 —	0.036 ± 0.005 —	95.93 ± 1.72 —	20.68 ± 1.11—
w/o SOI	0.759 ± 0.015 $p < 0.001$	0.056 ± 0.007 $p < 0.001$	0.044 ± 0.006 $p < 0.001$	92.87 ± 2.03 $p < 0.001$	19.96 ± 1.03 $p = 0.018$
w/o RVDA	0.731 ± 0.019 $p < 0.001$	0.069 ± 0.010 $p < 0.001$	0.061 ± 0.010 $p < 0.001$	89.60 ± 2.45 $p < 0.001$	17.89 ± 0.92 $p < 0.001$
w/o RL	0.747 ± 0.016 $p < 0.001$	0.061 ± 0.008 $p < 0.001$	0.049 ± 0.007 $p < 0.001$	92.07 ± 2.19 $p < 0.001$	18.42 ± 0.98 $p < 0.001$

Note: Values are reported as the mean ± standard deviation over 30 independent runs. The p-values were obtained using two-sided Wilcoxon rank-sum tests against SORD-RL-MOGWO and were adjusted using the Holm procedure for multiple comparisons. An adjusted p-value below 0.05 indicates a statistically significant difference. The symbols w/o SOI, w/o RVDA, and w/o RL denote the removal of Sobol–opposition initialization, reference-vector dual-archive management, and reinforcement learning, respectively.

To visualize the search preference before knee-point selection, Figure 10 presents the exploitation distribution of leader solutions in the PCA-projected design space. Figure 10 shows that most high-frequency leader selections are concentrated in the central feasible region, indicating that the reinforcement learning module preferentially exploits solutions that improve hypervolume. Meanwhile, several boundary solutions remain preserved by the dual-archive mechanism, maintaining Pareto-set diversity. The selected knee point lies within the main exploitation region and represents a balanced compromise among axial force, cutting torque, and chip-evacuation risk.

To comprehensively evaluate the solution performance of different optimization algorithms and the independent contributions of each improved module, the study compared SORD-RL-MOGWO with the comparison algorithms. The ablation configurations for removing Sobol - opposition learning initialization (w/o SOI), reference vector dual file management (w/o RVDA), and reinforcement learning policy conditioning (w/o RL) were constructed, and the results are shown in Table 5.

In Table 5, the hypervolume index of SORD-RL-MOGWO was 0.783±0.012, and the inverted generational distance, distribution uniformity, and feasible solution ratio were 0.047±0.006, 0.036±0.005, and 95.933±1.724%. The overall performance was superior to that of the comparison algorithms. Compared with MOGWO, its hypervolume index was increased by 13.64%, and the inverted generational distance and distribution uniformity were reduced by 48.352% and 51.351%, indicating that the improved strategy could enhance the convergence and distribution quality of the tool parameter scheme. Compared with DRLOS-EMCMO, the study method achieved better quality of the solution set and proportion of feasible solutions while reducing the running time by 12.829%, showing better solution efficiency. The ablation results indicated that the performance degradation was most significant after the removal of the reference vector dual file management, suggesting that the mechanism played a key role in coordinating low load, low chip risk and structural feasibility. The removal of the remaining modules also led to a decline in metrics, verifying the synergistic effectiveness of the three improved strategies. Although SORD-RL-MOGWO contains multiple enhancement mechanisms, their computational overhead is limited. Sobol-opposition sampling is performed only during initialization, reference-vector dual-archive management mainly involves normalization, association, and archive truncation, and the tabular Q-learning module updates only a small Q-table. In contrast, DRLOS-EMCMO requires repeated neural-network inference and parameter updates for operator selection. Therefore, under the same hardware and function-evaluation budget, SORD-RL-MOGWO achieves a shorter running time of 20.68 s than DRLOS-EMCMO at 23.73 s. The Wilcoxon rank-sum test results show that SORD-RL-MOGWO differed significantly from MOGWO, C-TAEA2, CMOEA-TSRA, and all ablated configurations in hypervolume, inverted generational distance, and spacing, with adjusted p-values below 0.05. Compared with DRLOS-EMCMO, significant differences were obtained for hypervolume, inverted generational distance, and spacing, whereas the difference in feasible solution ratio was not statistically significant after Holm correction, with an adjusted p-value of 0.085. This result indicates that the main advantage of SORD-RL-MOGWO over DRLOS-EMCMO lies in Pareto-front convergence and distribution quality rather than a statistically conclusive increase in the feasible solution ratio.

3.4. Manufacturing-Tolerance Sensitivity Analysis

To evaluate the engineering robustness of the selected knee-point design, a manufacturing-tolerance sensitivity analysis was conducted by independently perturbing the angular parameters by ±0.5° and ±1.0° and the dimensional parameters by ±0.01 mm and ±0.02 mm, as summarized in Table 6.

Table 6 shows that the selected knee-point geometry remains relatively robust under normal manufacturing tolerances. A deviation of ±0.5° or ±0.01 mm increases axial force by no more than 1.34% and chip-evacuation risk by no more than 1.89%. The edge radius is the most influential parameter for axial force, whereas the chip-breaker width and chip-groove guide angle have greater effects on chip-evacuation risk. Even under twice the normal tolerance, the maximum increases in axial force and chip-evacuation risk are limited to 2.71% and 4.72%, respectively.

Table 6. Manufacturing-tolerance sensitivity of the selected knee-point geometry

Parameter	Nominal value	Perturbation level	Worst-case deviation	Axial force (N)	Increase (%)	Chip-evacuation risk	Increase (%)
Knee-point design	—	0	—	1441.8 ± 10.6	0	0.212 ± 0.004	0
Rake angle	12.0°	±0.5°	−0.5°	1458.8 ± 11.0	1.18	0.213 ± 0.004	0.47
Parameter	Nominal value	Perturbation level	Worst-case deviation	Axial force (N)	Increase (%)	Chip-evacuation risk	Increase (%)
Rake angle	12.0°	±1.0°	−1.0°	1475.7 ± 11.7	2.35	0.215 ± 0.005	1.42
Clearance angle	8.0°	±0.5°	−0.5°	1454.5 ± 10.9	0.88	0.213 ± 0.004	0.47

Clearance angle	8.0°	±1.0°	−1.0°	1467.8 ± 11.5	1.8	0.214 ± 0.004	0.94
Point angle	118.0°	±0.5°	+0.5°	1455.8 ± 11.2	0.97	0.213 ± 0.004	0.47
Point angle	118.0°	±1.0°	+1.0°	1469.9 ± 11.6	1.95	0.214 ± 0.005	0.94
Edge radius	0.18 mm	±0.01 mm	+0.01 mm	1461.1 ± 11.6	1.34	0.214 ± 0.004	0.94
Edge radius	0.18 mm	±0.02 mm	+0.02 mm	1480.9 ± 12.4	2.71	0.217 ± 0.005	2.36
Chip-breaker width	1.20 mm	±0.01 mm	+0.01 mm	1448.7 ± 10.8	0.48	0.216 ± 0.005	1.89
Chip-breaker width	1.20 mm	±0.02 mm	+0.02 mm	1456.9 ± 11.3	1.05	0.221 ± 0.006	4.25
Chip-groove guide angle	24.0°	±0.5°	+0.5°	1449.3 ± 11.0	0.52	0.216 ± 0.005	1.89
Chip-groove guide angle	24.0°	±1.0°	+1.0°	1457.4 ± 11.8	1.08	0.222 ± 0.006	4.72

3.5. Actual Cutting Validation of Optimized Tools Under Multi-Machining Conditions

To evaluate the adaptability of the optimized tool geometries, cutting tests were conducted at feed rates of 0.040, 0.060, 0.080, and 0.100 mm/r, as shown in Figure 11. The tool denoted as “Original” in Figure 11 refers to the unoptimized baseline design established before geometric parameter optimization rather than a standard off-the-shelf industrial product. It used the same carbide insert material, tool-body structure, outer diameter, retained-core diameter, guide-pad arrangement, and internal-coolant configuration as the optimized tool. The two tools differed only in the six optimized geometric parameters, namely the rake angle, clearance angle, point angle, edge radius, chip-breaker width, and chip-groove guide angle. Because chip blockage is a binary event, its uncertainty was quantified using the 95% Wilson confidence interval. Differences between the original and optimized tools were evaluated using a two-sided Fisher’s exact test, with statistical significance defined at $p<0.05$.

In Figure 11 (a), the axial force of the SORD-RL-MOGWO optimized tool under high feed conditions was 1814 N, which was 14.232% lower than that of the original tool, indicating that the optimized cutting-edge structure could effectively reduce the axial cutting load. In Figure 11 (b), the cutting torque of the tool was 19.480 N·m, which was 13.996% lower than that of the original tool, indicating that the optimization of the rake face and chip diversion structure helped to improve the chip flow state. Figure 11(c) shows that, at 0.040 mm/r, the optimized tool reduced axial force and cutting torque by approximately 12% and 9%, respectively, while the chip-blockage rate decreased from 5% to 0%. At 0.100 mm/r, chip blockage occurred in 11 of 20 trials for the original tool and 4 of 20 trials for the optimized tool. The corresponding blockage rates were 55.0% with a 95% confidence interval of 34.2%–74.2% and 20.0% with a 95% confidence interval of 8.1%–41.6%, respectively. The absolute reduction was 35.0 percentage points with a 95% confidence interval of 5.0–57.6 percentage points, and the difference reached statistical significance according to Fisher’s exact test, with $p=0.048$.

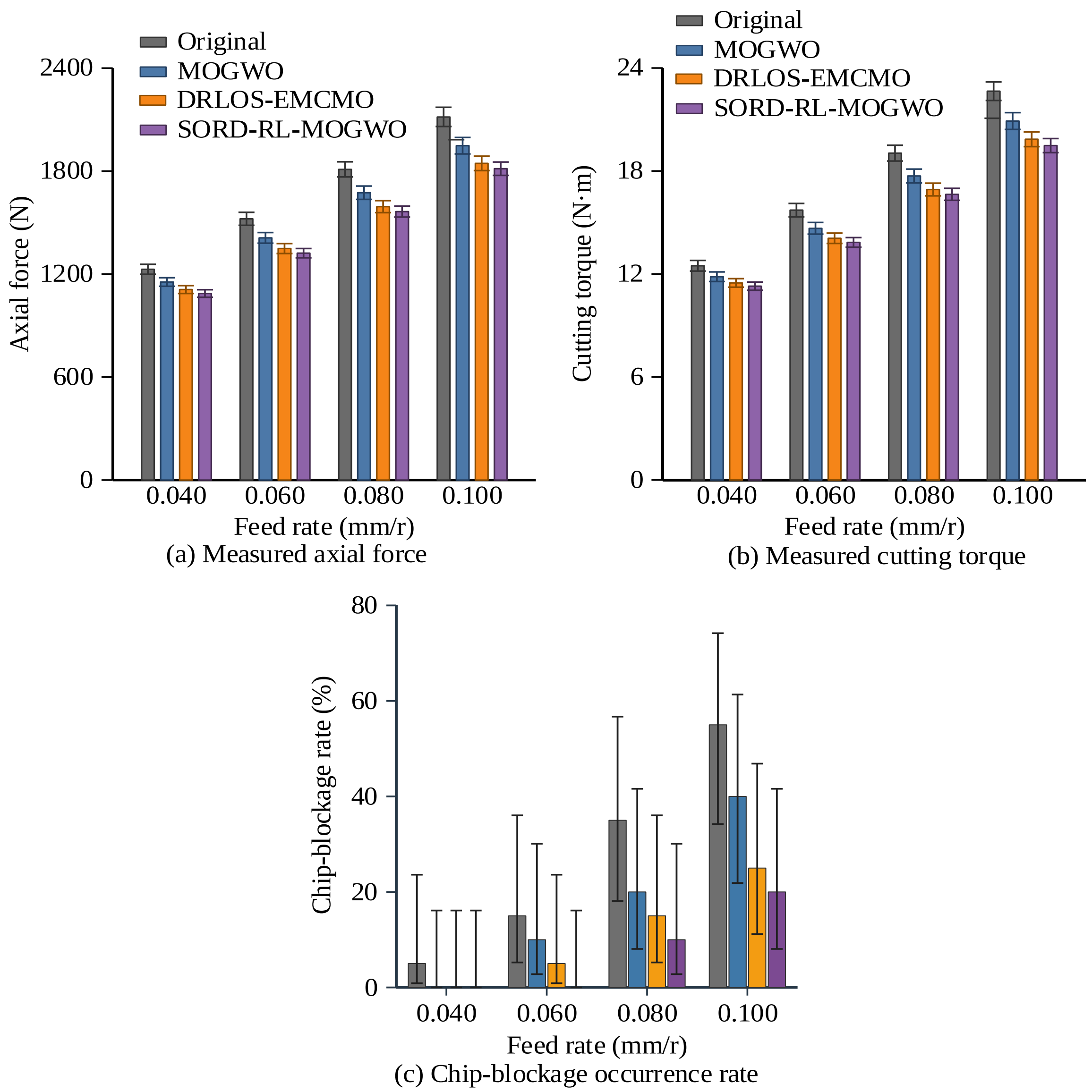

Fig. 11. Verification results of optimized tool cutting under different machining conditions (Error bars in (a) and (b): standard deviation over five repeated tests; error bars in (c): 95% Wilson confidence intervals over 20 trials.)

Table 7. Cutting-load fluctuations of the original and optimized tools

Feed rate (mm·r^{-1})	Tool	Mean axial force (N)	Axial-force signal SD (N)	Axial-force CV (%)	Mean torque (N·m)	Torque signal SD (N·m)	Torque CV (%)
0.04	Original	1268	58.3	4.6	14.18	0.57	4.02
0.04	Optimized	1116	35.7	3.2	12.91	0.37	2.87
0.06	Original	1564	84.5	5.4	17.03	0.79	4.64
0.06	Optimized	1372	49.4	3.6	15.34	0.49	3.19
0.08	Original	1847	116.4	6.3	19.86	1.05	5.29
0.08	Optimized	1602	67.3	4.2	17.49	0.65	3.72
0.1	Original	2115	150.2	7.1	22.65	1.36	6.00
0.1	Optimized	1814	81.6	4.5	19.48	0.80	4.11

To further evaluate the dynamic cutting stability of the optimized geometry, the fluctuation characteristics of the stable-stage load signals were analyzed at different feed rates. Entry transients were removed, and identical filtering parameters and sampling windows were applied to both tools. The signal standard deviation and coefficient of variation were calculated from five repeated tests under each condition, as shown in Table 7. Table 7 shows that the optimized tool consistently reduces both the mean load and signal fluctuation. At 0.100 mm/r, the axial-force standard deviation decreases from 150.2 N to 81.6 N, corresponding to a reduction of 45.7%, while the torque standard deviation decreases from 1.36 N·m to 0.80 N·m, a reduction of 41.2%. The axial-force coefficient of variation also decreases from 7.10% to 4.50%. These results indicate that the optimized geometry suppresses intermittent chip impact and load fluctuations, thereby improving cutting stability under high-feed conditions. However, its influence on tool life should be further verified through long-duration wear tests.

4. Conclusion

This study addressed the high cutting load, unstable chip evacuation, and coupled geometric design challenges of deep-hole trepanning tools by establishing a multi-objective optimization framework that simultaneously considers axial force, cutting torque, chip-evacuation risk, and structural feasibility. Beyond numerical performance, SORD-RL-MOGWO identified diverse and manufacturable solutions within the narrow feasible design space, enabling coordinated control of cutting load, chip evacuation, and structural safety. Its practical value lies in supporting geometry screening before physical cutting tests and providing alternative Pareto-optimal designs for different engineering requirements.

Experiments showed that the load evaluation model had determination coefficients of 0.983 for axial force and 0.990 for cutting torque. The hypervolume index of the complete algorithm was 0.783±0.012, the inverted generational distance was 0.047±0.006, and the proportion of feasible solutions was 95.933±1.724%. At a feed rate of 0.100 mm/r, the optimized tool reduced axial force and cutting torque by 14.232% and 13.996%, respectively, while the chip blockage rate decreased by 35 percentage points, from 55.0% to 20.0%. The substantial reduction in chip blockage can alleviate repeated chip impact, local heat accumulation, and abnormal load fluctuations, which is expected to reduce cutting-edge damage and unplanned interruptions, thereby improving tool service life and long-term process reliability in deep-hole trepanning. These results indicate that the model can reliably screen candidate geometries before physical cutting tests. By eliminating infeasible or high-load designs at the optimization stage, the proposed framework can reduce repeated trial machining, shorten the parameter-selection cycle, and limit unnecessary tool and material consumption in engineering applications.

The ablation results further show that reference-vector dual-archive management makes the largest contribution to Pareto-front quality among the three enhancement modules. Removing this mechanism reduced the hypervolume from 0.783 to 0.731, a decrease of 6.64%, and produced the most pronounced deterioration in convergence, distribution uniformity, and feasible-solution coverage. This finding confirms that coordinated management of the convergence and diversity archives is the key mechanism enabling SORD-RL-MOGWO to maintain well-distributed feasible solutions within the narrow and highly constrained design space.

Tool-wear evolution was excluded because the study focuses on initial geometry optimization and aims to isolate geometric effects from progressive edge degradation. Although the SORD-RL-MOGWO framework is generally applicable, transferring the model from GH4169 to stainless steels or titanium alloys requires recalibration of the cutting coefficients, chip-evacuation thresholds, and feasible geometric ranges. Future work will therefore include wear-dependent optimization, multi-batch and multi-material validation, temperature and coolant-flow measurements, and verification under higher-load cutting conditions.

Acknowledgement

The research is supported by School Grants platform for Scientific Research of Shandong Huayu University of Technology in 2025: CNC tool manufacturing process research and development center, PT2025KJX001.

References

[1] [De Melo Pereira L A, Santos S C, Martins P S, et al. Chip formation analysis while drilling Al-Mg-Si 6061-T6 alloy using high-speed steel drills with and without DLC. The International Journal of Advanced Manufacturing Technology, 2026, 142(9-10): 5213-5231. https://doi.org/10.1007/s00170-025-17345-2

[2] Qin Y, Liu Y, Guan W, et al. Ultrasonic assisted electrochemical drilling and grinding of small holes on SLMed Hastelloy X with rotating abrasive tube electrode. The International Journal of Advanced Manufacturing Technology, 2024, 130(11-12): 5181-5197. https://doi.org/10.1007/s00170-024-12978-1.

[3] .Sristi N A, Zaman P B. A review of textured cutting tools' impact on machining performance from a tribological perspective. The International Journal of Advanced Manufacturing Technology, 2024, 133(9-10): 4023-4057. https://doi.org/10.1007/s00170-024-13865-5

[4] Gao C H, Cheng K, Kirkwood D. The investigation on the machining process of BTA deep hole drilling. Journal of Materials Processing Technology, 2000, 107(1-3): 222-227. https://doi.org/10.1016/S0924-0136(00)00684-1

[5] Richardson R, Bhatti R. A review of research into the role of guide pads in BTA deep-hole machining. Journal of Materials Processing Technology, 2001, 110(1): 61-69. https://doi.org/10.1016/S0924-0136(00)00733-0

[6] Strodick S, Schmidt R, Donnerbauer K, et al. Subsurface conditioning in BTA deep hole drilling for improved component performance. Production Engineering, 2024, 18(2): 299-317. https://doi.org/10.1007/s11740-023-01252-0

[7] Wegert R, Guski V, Schmauder S, et al. In-process approach for editing the subsurface properties during single-lip deep hole drilling using a sensor-integrated tool. Production Engineering, 2024, 18(2): 319-337. https://doi.org/10.1007/s11740-024-01265-3

[8] Atif M, Wang X, Xie L, et al. Influence of cutting tool design on ultrasonic-assisted drilling of fiber metal laminates. The International Journal of Advanced Manufacturing Technology, 2024, 131(12): 6039-6059. https://doi.org/10.1007/s00170-024-13128-3

[9] Jia J, Wang Q, Lei Y, et al. Cathode design and structure optimization of the ECM for special-shaped deep holes. The International Journal of Advanced Manufacturing Technology, 2024, 131(9-10): 4403-4423. https://doi.org/10.1007/s00170-024-13296-2

[10] Qiao K, Liang J, Yu K, et al. Evolutionary constrained multiobjective optimization: Scalable high-dimensional constraint benchmarks and algorithm. IEEE Transactions on Evolutionary Computation, 2024, 28 (4) : 965-979. https://doi.org/10.1109 / TEVC. 2023.3281666

[11] Rupasinghe N, Michel S, Baumann A, Gerken J, Gülde S, Biermann D, Eberhard P. Numerical and experimental evaluation of chip evacuation and lubricant flow using optimized drill heads for ejector deep hole drilling. Production Engineering, 2026, 20(2): 52. https://doi.org/10.1007/s11740-025-01406-2

[12] Zheng J, Chen S. A Q-learning multi-objective grey wolf optimizer for the distributed hybrid flowshop scheduling problem. Engineering Optimization, 2025, 57 (9) : 2609-2628. https://doi.org/10.1080/0305215X.2024.2410844

[13] Wu R, Huang S, Zhang W, et al. An improved grey wolf optimizer for minimizing drilling deformation and residual stress in AA2024 sheet. The International Journal of Advanced Manufacturing Technology, 2024, 130(9-10): 4443-4458. https://doi.org/10.1007/s00170-023-12905-w

[14] Wang K, Sun Q, Yang H, et al. Drilling performance of small holes on C_f/SiC composites with brazed diamond grinding rods. The International Journal of Advanced Manufacturing Technology, 2024, 133(11-12): 5485-5500. https://doi.org/10.1007/s00170-024-14013-9

[15] Zhang R, Liang Z, Yi L, Hu J, Du Y, Guo L, Ma Y, Cai R, Zhao Q, Xiong L. Research on the design and cutting performance of a novel BTA boring tool intended for machining of nickel-based superalloys. Journal of Materials Research and Technology, 2025, 36:7980-7995. https://doi.org/10.1016/j.jmrt.2025.05.022

[16] Biermann D, Kersting M, Kessler N. Process adapted structure optimization of deep hole drilling tools. CIRP Annals, 2009, 58(1): 89-92. https://doi.org/10.1016/j.cirp.2009.03.102

[17] Biermann D, Bleicher F, Heisel U, Klocke F, Möhring H-C, Shih A. Deep hole drilling. CIRP Annals, 2018, 67(2): 673-694. https://doi.org/10.1016/j.cirp.2018.05.007

[18] Waqas M, Naseem A. Artificial intelligence in sustainable industrial transformation: a comparative study of industry 4.0 and industry 5.0. FinTech and Sustainable Innovation, 2025, 1: A2. https://doi.org/10.47852 / bonviewFSI52025321
[19] Sobol I M. On the distribution of points in a cube and the approximate evaluation of integrals. USSR Computational Mathematics and Mathematical Physics, 1967, 7(4): 86–112. https://doi.org/10.1016/0041-5553(67)90144-9
[20] Tizhoosh H R. Opposition-based learning: A new scheme for machine intelligence. Proceedings of the International Conference on Computational Intelligence for Modelling, Control and Automation and International Conference on Intelligent Agents, Web Technologies and Internet Commerce, 2005, 1: 695–701. https://doi.org/10.1109/CIMCA.2005.1631345
[21] Cheng R, Jin Y, Olhofer M, Sendhoff B. A reference vector guided evolutionary algorithm for many-objective optimization. IEEE Transactions on Evolutionary Computation, 2016, 20(5): 773–791. https://doi.org/10.1109/TEVC.2016.2519378
[22] Li K, Chen R, Fu G, Yao X. Two-archive evolutionary algorithm for constrained multiobjective optimization. IEEE Transactions on Evolutionary Computation, 2019, 23(2): 303–315. https://doi.org/10.1109/TEVC.2018.2855411
[23] Li W, Gong W, Ming F, Wang L. Constrained multi-objective evolutionary algorithm with an improved two-archive strategy. Knowledge-Based Systems, 2022, 246: 108732. https://doi.org/10.1016/j.knosys.2022.108732
[24] Xia M, Chong Q, Dong M. A constrained multi-objective evolutionary algorithm with two-stage resources allocation. Swarm and Evolutionary Computation, 2023, 79: 101313. https://doi.org/10.1016/j.swevo.2023.101313
[25] Ming F, Gong W, Wang L, Jin Y. Constrained multi-objective optimization with deep reinforcement learning assisted operator selection. IEEE/CAA Journal of Automatica Sinica, 2024, 11(4): 919–931. https://doi.org/10.1109/JAS.2023.123687